Applied Thermal Engineering 196 (2021) 117345

Contents lists available at ScienceDirect

Applied Thermal Engineering

journal homepage: www.elsevier.com/locate/apthermeng

Design a cooling pillow to support a high-speed supercritical CO_2 turbine shaft

Md. Uddin [a,*], Halim Gurgenci [a], Zhiqiang Guan [a], Alex Klimenko [a], Jun Li [b], Jishun Li [b], Lun Li [b]

[a] School of Mechanical and Mining Engineering, University of Queensland, St Lucia, Queensland 4072, Australia

[b] Department of Mechanical Engineering, Henan University of Science and Technology, Luoyang, China

ARTICLE INFO

Keywords:
Cooling Pillow
Cooling capacity
Rotor dynamics
Trade-offs
Supercritical CO_2 turbine

ABSTRACT

Supercritical CO_2 cycles offer a new thermal power generation paradigm but their commercial deployment has been slow due to significant turbine design challenges. Rotor bearings and seal design are identified as the critical challenges due to the high temperatures, high pressures, and high rotational speeds, a combination of extreme values not encountered in any other past turbine applications. This paper presents a new supercritical CO_2 turbine configuration that addresses these challenges by introducing a rotor shaft cooling zone to control the temperatures encountered by the seals and the bearings. This makes it possible to use proven conventional seal and bearing technology. The salient feature is referred to as a 'cooling pillow' that cools the rotor shaft to a tolerable seal temperature by circulating supercritical CO_2 fluid through the annulus and at the same time provides dynamic support to the rotating shaft against vibration. Turbulent heat transfer and frictional heat generation correlations for the annuli have been employed to evaluate the cooling performance and the simplified Reynolds equation for hydrodynamic fluid film lubrication has been employed to evaluate the dynamic performance. Design charts and figures are presented using non-dimensional parameters to help with the design of supercritical CO_2 turbines at different temperatures and sizes. The COMSOL rotor-bearing system simulator consisting of bearing and disks with the main shaft has been employed to produce Campbell plots and carry out a parametric study of rotor vibration frequencies varying with the cooling zone design. The cooling capacity is found to be significantly higher than the cooling load required. Moreover, the convection heat transfer coefficient and dimensionless temperature distribution are independent of radial clearance and this offers trade-offs in terms of controlling rotor vibrations. Through the pursuit of such trade-offs, it is demonstrated that dynamic performance can be improved by up to 55% and 60% for the 0.5 MW and 10 MW turbine sizes, respectively.

1. Introduction

Electricity has been the main power carrier for over a century and it is difficult to think of a feature of modern civilization that is feasible without it. Two-thirds of the world's electricity is produced by burning fossil fuels [1]. Fossil fuels have dominated the electricity generation industry since its early days. This may be changing now with fossil fuels getting replaced by other sources. Reasons for this change include resource limitations, environmental implications, climate change impact, and advances in renewable energy technology.

A significant advance in thermal power generation in recent years has been high-temperature high-efficiency power cycles such as the supercritical CO_2 cycle. The supercritical CO_2 Brayton cycle was referred to as a step-change transformational electricity production method by the US Department of Energy and is generally accepted as the next-generation technology in a diverse range of applications including nuclear power generation, fossil fuel power generation, and concentrated solar power [2–6]. In this cycle, CO_2 is used as the working fluid and its pressure and temperature are maintained above the critical point (7.39 MPa and 31.1 degrees Celsius). Carbon dioxide is the most appropriate fluid for this cycle due to its near-ambient critical temperature and relatively low critical pressure. It is also stable, inert at a wider range of temperature, non-toxic and, inexpensive. Unlike steam Rankine cycles, a supercritical CO_2 Brayton cycle can operate at very high temperatures and manageable pressure ratios. The downside in any Brayton cycle is the high compression work but this can be minimized in a supercritical CO_2 Brayton cycle due to low compressibility and high fluid density near

* Corresponding author.
E-mail address: m.uddin@uq.net.au (Md. Uddin).

https://doi.org/10.1016/j.applthermaleng.2021.117345
Received 17 April 2021; Received in revised form 19 June 2021; Accepted 11 July 2021
Available online 15 July 2021
1359-4311/

Nomenclature

a	Cooling length factor
b	Bearing spacing factor
C	Radial clearance (m)
C_p	Specific heat (J/kg.K)
D	The diameter of the shaft (m)
D_h	Hydraulic diameter (m)
e	Eccentricity (m)
ε	Eccentricity ratio (e/C)
E	Modulus of elasticity (N/m^2)
h	Convection heat transfer co-efficient ($W/m^2.k$)
I	Area moment of inertia (m^4)
k	Thermal conductivity of the materials (W/m.K)
k_f	Fluid heat conductance (W/m.K)
K	Stiffness (N/m)
Nu	Nusselt number
Pr	Prandtl number
Q_f	Frictional heat (Watt)
Q_c	Conducted heat (Watt)
R, R_1	Shaft radius (m)
Re_a	Axial Reynolds number
T	Temperature
Ta	Taylor Number
μ	Dynamic viscosity of the fluid (Pa.s)
υ	Kinematic viscosity of the fluid (m^2/s)
V_a	The axial velocity of the fluid (m/s)
V_0	The linear velocity of the shaft (m/s)
ω	Angular velocity of the shaft (rad/s)
λ	Dimensionless parameter
σ	Stefan Boltzmann constant ($W/m^{-2}.K^{-4}$)
ν	Kinematic viscosity

the critical point [7]. The supercritical CO_2 cycle is being proposed for a variety of applications but the main motivation for the authors is its use in Concentrating Solar Thermal (CST) power generation. It has been over ten years since the supercritical CO_2 Brayton cycle has been proposed as a critical step-change for CST [8–9] due to its high efficiency and smaller size compared to the conventional steam cycle.

Supercritical CO_2 cycle layouts have been studied extensively [10–14]. The supercritical CO_2 turbine blade design, impeller design, compressor design, feasibility at different operating conditions, material choice, aerodynamic and mechanical design, and their performance were also investigated in relatively recent literature [15–18]. Regardless of all this effort, notwithstanding several laboratory-scale tests, there is not yet a commercial supercritical CO_2 turbine. The technology has not advanced beyond the lab-scale test rigs in the USA, Mexico, Japan, Korea [19]. Two notable studies identified significant challenges in supercritical CO_2 power block technology [20–21]. The Tokyo Institute of Technology identified the bearing and seal design are the critical challenges for the supercritical CO_2 turbine [22]. The exceptional confluence of high temperatures, high pressures, and high rotational speeds are the reason [23]. Table 1 shows how the supercritical CO_2 turbine fosters challenges over the existing turbine system in terms of temperature, pressure, and rotational speed.

Alexander et al. 2018 [18] investigated the suitability of roller bearings, foil bearings, and magnetic bearings in supercritical CO_2 turbine design. While magnetic bearings remain to be an option, their additional complexity (actuator, sensor, bearing controller, etc.) requires further investigations before they can be incorporated into a supercritical CO_2 turbine design. Foil bearings offer limited thrust capacity and roller bearings are also not favored due to the high rotational speeds such turbines are expected to operate. Hydrodynamic or hydrostatic oil-lubricated bearings offer a suitable solution in terms of their load and speed capability but they cannot be subjected to high temperatures and need to be isolated from high-temperature by using appropriate sealing arrangements. The additional concern of high-density fluid at high pressure in the bearing passage combined with high temperature and high-speed condition creates stability issues and high windage losses [23]. Some common sealing components and materials such as propylene, O-rings, ethylene, monomer, diene, and rubber were found as unsuitable for supercritical CO_2 as their use was restricted to temperatures below 100 degrees Celsius. Instead, labyrinth seals (LAB) and dry gas seals (DGS) were reported as suitable. The present dry gas seal technology is limited to maximum temperatures below 200 degrees Celsius [27]. While using the dry gas seal, it should be noted that the shaft temperature is required to keep within the dry gas seal temperature limit. Aaron et al. 2018 [28] focus on the design of the supercritical CO_2 turbine seal and test rig. Film riding face seal technology was also recommended for supercritical CO_2 turbine design. Such a type of seal is currently under the development phase.

Table 1
The supercritical CO_2 turbine over the existing turbine system [23–26].

Parameters	Gas turbine	Steam turbine	Supercritical CO_2 turbine
Turbine inlet temperature, °C	>1,000	<600	700
Maximum Pressure, MPa	<3	30	22
Rotational speed, RPM	3,000–3,600	2,600–3,000	30,000

Past literature suggests that new bearing seal and bearing technology to operate in the high-temperature high-pressure gas region has not been feasible. Proven bearing and seal technologies offer the only feasible option but this means the hot gas needs to be confined behind temperature and pressure barriers, and the seals and bearings should be protected against hot metal temperatures. Addressing the above challenges the University of Queensland (UQ) designed a modular and scalable supercritical CO_2 radial in-flow turbine configuration (Fig. 1) with size ranges from 1-MW to 30-MW for the CST application, which is the subject of this study [5]. The turbine provides temperature and pressure isolation using two seals. The seal closest to the rotor is a labyrinth seal that confines the high-temperature fluid but not the pressure. The second seal is a dry gas seal that confines the pressure. The labyrinth seal protects the dry gas seal against contact with high-temperature gas. However, the seal is still in contact with the rotor shaft. Therefore, to keep the dry gas seal temperatures tolerable, a cooling zone length was included between the dry gas seal and the labyrinth seal to limit the rotor shaft temperature, which cools the shaft by a circulating cooling stream. The necessity of a shaft cooling zone length is not only for the UQ turbine but for all supercritical CO_2 turbines employing conventional seals and bearings.

While solving the seal protection problem, the cooling zone introduces additional unsupported shaft length, which may cause vibration problems, a situation that is already of concern due to the high rotational speeds employed by such turbines. Swann and Russell [29] analyzed the structural heat transfer for a small size (100 kW) concept design of supercritical CO_2 turbine shaft-cooling zone along with the shaft materials for a given condition. This study aims to present a parametric model for the cooling zone design and investigate the possible intrinsic dual functionality including cooling and dynamic support simultaneously on the rotating shaft. This is a novel approach and has the potential to remove the main stumbling block that is preventing commercial deployment of supercritical CO_2 turbine technology.

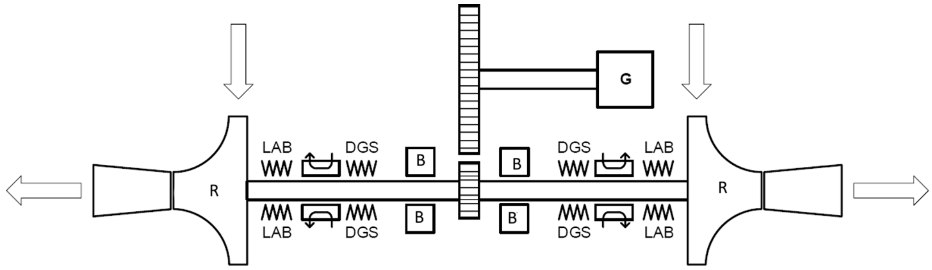

Fig. 1. Supercritical CO_2 radial-in-flow turbine full layout [29].

2. Problem definition, geometry, and boundary conditions

The operation of the shaft cooling zone cannot be examined in isolation and it needs to be presented as a component in a turbine design. A generic radial turbine is introduced here so that the paper becomes useful to other high-temperature supercritical CO_2 turbine designers.

2.1. The problem layout and setup

The radial turbine rotor shaft with essential elements includes labyrinth seal, cooling length, dry gas seal, and bearings are shown in Fig. 2. The labyrinth seal is placed near the rotor and the dry gas seal is placed near the bearing. The dry gas seal is not in contact with the hot-temperature gas but is in contact with the rotor shaft. The rotor shaft is subject to the turbine inlet temperature at its rotor end and needs to be cooled. The cooling length between the labyrinth and dry gas seals is an annulus outside a fast-rotating shaft. A cooler stream of supercritical CO_2 cycle fluid circulates through this length at a pressure high enough to prevent leakage from the labyrinth seal. Supercritical CO_2 is a good cooling fluid choice due to its high heat transfer characteristics as a coolant [29]. The thermal management in the casing is also important but is easier to manage due to the lack of sliding contacts and is not considered in this paper.

The origin of the x-axis is set at the rotor wheel center of mass. The location of the center of mass and all other component widths has been defined in terms of the shaft diameter, D, as listed in Table 2. The definitions in Table 2 may show slight variations between different turbine designs depending on the aerodynamic design method employed, boundary conditions, and the target shaft power. In a first-pass analysis, these differences may be ignored.

Table 2
Location of the components and their widths.

Parameter	Description	Average value	Reference
x_1	The rotor wheel center of mass	0.40 D	[30]
x_2-x_1	Labyrinth seal width	0.22 D	[31–32]
x_3-x_2	Cooling zone length	aD	This paper
x_4-x_3	Dry gas seal width	0.26 D	[27,33–34]
x_5-x_4	Bearing width	0.70 D	[35–37]
x_6-x_5	Bearing separation	bD	The bearing separation, b, is a value to be set by the designer based on the gearbox design.
x_7-x_6	Bearing width	0.70 D	As in x_5-x_4

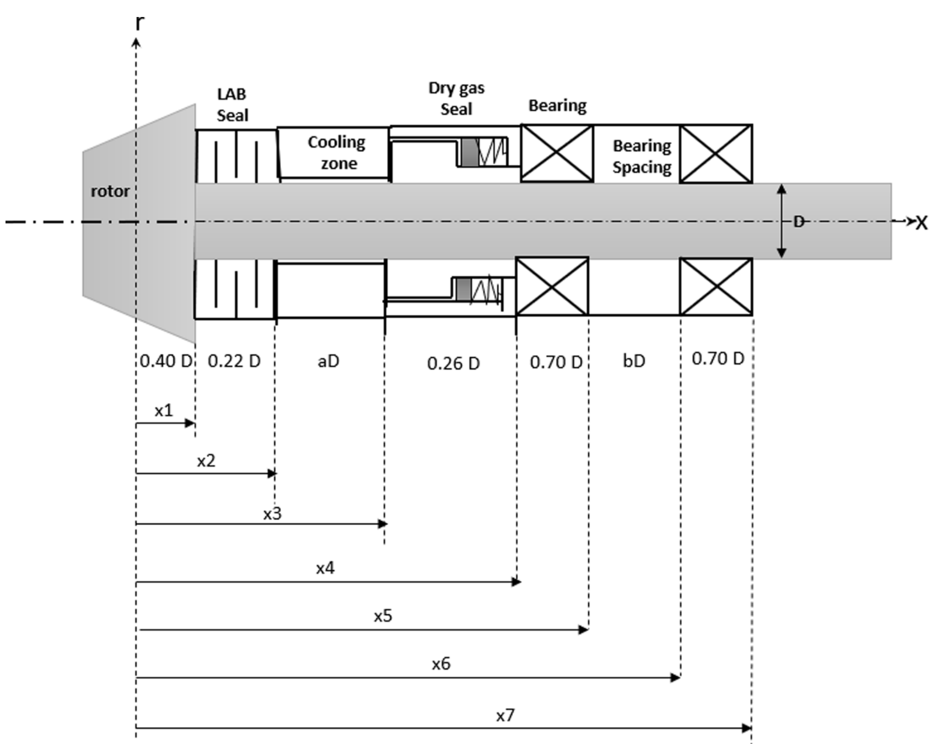

Fig. 2. Radial turbine rotor support essential elements and critical parameters.

2.2. The boundary condition and assumptions

In designing a radial turbine, some invariants are dictated by the present seal bearing technology, e.g. the maximum allowable shaft perimeter velocity(u_{max}) and maximum allowable shaft temperature at the dry gas seal boundary(T_{dgs}). The following section should apply to supercritical CO_2 turbines of arbitrary turbine inlet temperature and rotational speed as long as these constraints are observed. The temperature and velocity boundary conditions are given in Table 3. The reference temperature, T_o, is an invariant dictated by the present seal technology.

The shaft diameter, D, is a degree of freedom available to the designer. The author assumed that it is equal to the rotor exit diameter. The rotor can be designed by several mean line design methods offered in the literature. Sangkyoung and Hal [30] offer a comparative analysis of these methods and compares their design outputs at a power range of 0.3–10 MW. In terms of the rotor exit radius, the differences between different design processes are not different. Therefore, the author assumed that the values listed in Table 4 applicable to any radial supercritical CO_2 turbine design subject to the constraints already mentioned.

Finally, an assumption needs to be made on the shaft material. Steel is not an option at the temperatures usually targeted with supercritical CO_2 cycles and nickel-based alloys such as Inconel are used. Inconel thermal conductivities vary only slightly with the grade and a value of 22 W/m-K, which is the thermal conductivity reported in the literature for Inconel 625 annealed [38] and Inconel 718 aged [39] at a temperature of 700 degrees Celsius and can be used as an approximate value for other Inconel alloys.

3. Thermal analysis

Referring to Fig. 2, the purpose of the cooling zone is to make sure that the temperature T_3 at x_3 is lower than T_o. This is achieved by circulating cool supercritical CO_2 through the cooling zone. The heat load that needs to be removed has two components, the conducted heat (Q_c) and the frictionally generated heat (Q_f). Assuming the interior temperature of the shaft remains essentially uniform during the heat transfer, the integral conduction heat load can be expressed as follows.

$$Q_c = k\frac{\pi D^2}{4}\left(\frac{T_2 - T_3}{x_3 - x_2}\right) = \frac{\pi k}{4}\frac{D(T_H - T_0)}{a} \tag{1}$$

where $a = \frac{x_3 - x_2}{D}$.

At the cooling flow rates of interest, the frictional heat generation due to axial travel can be ignored compared to rotational heat generation, provided the clearance is not too small. For the frictional heat generation in turbulent rotating flow in an annulus, different correlations exist in the literature, including Peter [40], Ralph [41], and James [42]. They all have the common form as

$$Q_f = C_g \rho \omega^3 D^4 L_c = C_g \rho \omega^3 D^5 a \tag{2}$$

and by using the definition of the limiting velocity, $V_0 = \omega R$ with V_0 as defined in Table 3,

$$Q_f = C_g \rho V_0^3 D^2 a \tag{3}$$

Fig. 3 plots the ratio of the conducted heat to frictional dissipation against the cooling zone length. For very small cooling zone lengths ($a <$ 0.10), the conduction heat load dominates. However, such short lengths are not sufficient to dispose of the heat receiving from the turbine backplane through conduction. For very large cooling zone lengths ($a >$ 2), the effect of the conduction heat load is negligible. A long cooling zone is not desirable because of its damaging effect on shaft vibrations. For the cooling zone lengths in between, need to consider both conduction and frictional heat loads.

Critical to an accurate determination of the cooling zone length is the value of the heat transfer coefficient. The heat transport mechanisms are complex in this annulus region around the fast-rotating shaft confined by the stationary boundary. The annulus clearance is very small compared to its length and the shaft is rotating. Therefore temperature variation normal to the flow and in the angular direction is assumed to be insignificant. At high enough speeds, so-called Taylor vortices are generated. The dimensionless heat transfer coefficient, the Nusselt number, can be expressed as a function of Taylor, Prandtl, and Reynolds numbers.

A comprehensive review of the past heat transfer studies at different Taylor number ranges is provided by Fenote et al [43]. The Taylor number is similar to Reynold's number in the sense that it represents the ratio between the inertial and viscous effects, except that in the Taylor number, the inertia considered is the rotational inertia. Different Taylor number definitions have been offered in the literature, the author used the definition from Fenote et al:

$$Ta = \frac{\omega^2 R_1 (D_h/2)^3}{\upsilon^2} \tag{4}$$

Table 3
Temperature and velocity boundary conditions.

Parameter	Description	Value	Reference
T_1	Stator exit temperature	T_H	This is related to the Turbine inlet temperature, TIT, through the stator nozzle design. In this paper, it is assumed to be equal to TIT
T_2	The temperature at the edge of the labyrinth seal	T_C	The coolant inlet temperature is assumed to be 100 degrees Celsius.
T_3	The temperature at the end of the cooling zone	T_o	200 degrees Celsius, set by the dry gas seal conditions and not expected to be relaxed in the near future
V	The shaft linear speed ($=\omega R_1$)	V_o<=120 m/s	Limited by the present dry gas seal technology

Table 4
The assumed variation of the shaft diameter with power (assuming the shaft diameter is equal to the rotor exit diameter).

Power (MW)	Shaft diameter, D (mm)	Angular velocity, ω (rad/s)
0.5	76	3141
1.0	81	2827
10	252	900

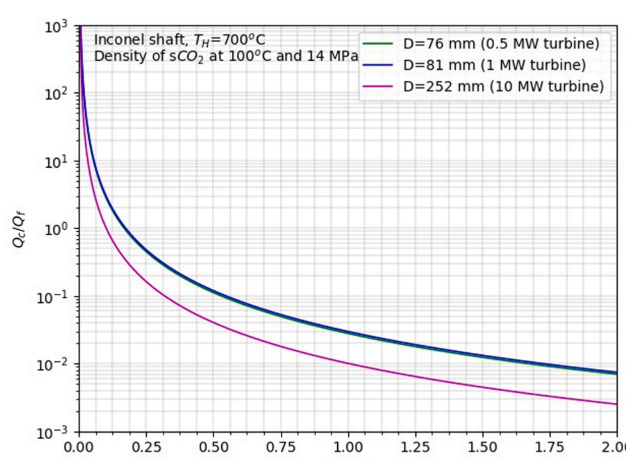

Fig. 3. The relative magnitude of conduction and frictional heat load at different shaft diameters.

where the hydraulic diameter is

$$D_h = \frac{4S_p}{P_m} = \frac{2\,[\pi(R_2^2 - R_1^2)]}{\pi(R_2 + R_1)} = 2\,(R_2 - R_1) = 2C \tag{5}$$

Combining the two equations and substituting the velocity boundary condition from Table 3, obtain:

$$Ta = \frac{V_0^2\,(R_2 - R_1)^3}{\upsilon^2 R_1} = \frac{V_0^2\,C^3}{\upsilon^2 R_1} \tag{6}$$

The Taylor number is strongly influenced by the value of the clearance (R_2-R_1). The lower limit for this parameter is the clearances encountered in hydrodynamic bearings, (R_2-R_1) $>$ 0.001R_1 [38]. By substituting into Eq. (6) C = 0.001R_1, CO_2 properties at T_0, the velocity boundary condition in Table 3, and the shaft radius range given in Table 4, the minimum value for the Taylor number as Ta $> 9.6 \times 10^5$-10.6×10^6.

For Ta numbers above this range, Fenote et al offer the following heat transfer correlations for the radial heat transfer:

$$Nu = 0.092\,(TaPr)^{1/3} \qquad [Ta = 1\times10^8 - 5\times10^{12}] \tag{7}$$

$$Nu = 0.42\,(TaPr)^{0.25} \qquad [Ta = up\ to\ 1\times10^8] \tag{8}$$

$$Nu = 8.854\,\left(\frac{R_1\omega e}{\upsilon}\right)^{0.262}(Pr)^{0.4} \qquad [e = 0.12\,R_1;\ \ Ta = 8\times10^3 - 2\times10^8] \tag{9}$$

With the Nusselt number defined as Nu = hD_h/k_f = $2hC/k_f$ and noting that $R_1 = D/2$, the Eq. (7) delivers a heat transfer coefficient as

$$h = C_h/D^{1/3} \tag{10}$$

Where C_h is a coefficient that only depends on the fluid properties:

$$C_h = 0.092\times1.26\left(\frac{V_0^2 k_f^3 Pr}{\upsilon^2}\right)^{1/3} = 0.116\left(\frac{V_0^2 k_f^3 Pr}{\upsilon^2}\right)^{1/3}\ \ (\mathrm{W/m^{5/3}{\cdot}K}) \tag{11}$$

The velocity V_o is a constant representing the technology constraints as defined in Table 3.

The above heat transfer correlations are valid for relatively low axial Reynolds numbers. Following the advice given in Fenote et al [43], an axial Reynolds number of $Re_a = V_a D_h/\upsilon = 2.5\times10^4$ is adopted and the flow rates to maintain this axial Reynolds number computed for 1 mm clearance and at different turbine sizes, namely 0.080, 0.085, and 0.263 kg/s for the 0.5 MW, 1 MW and 10 MW rotors, respectively.

Once the approximation for the heat transfer coefficient, h obtain, the temperature distribution along the cooling zone can be determined by solving the one-dimensional conduction equation subject to cooling on its surface:

Referring to Fig. 4, the governing energy balance simplified equation can be written as:

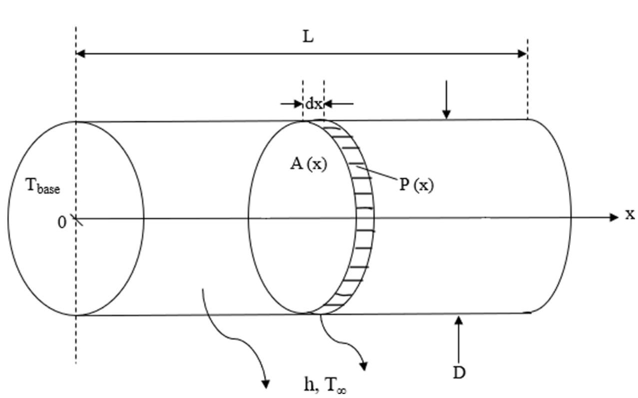

Fig. 4. Nomenclature for the differential heat conduction equation.

$$\frac{d^2T}{dx^2}dx = \frac{4h}{kD}(T - T_\infty)dx - \frac{Q_f}{kA} + \frac{4\sigma}{kD}(T^4 - T_\infty^4)dx \tag{12}$$

The last term in this equation is radiative loss. For temperatures presently considered for this application, this term is relatively small. Fig. 5 shows the ratio of the convective to radiative loss terms for unit length at different surface temperatures. For a low temperature (<600 degrees Celsius), the radiation heat loss is less than 0.6% of the total loss even for the largest rotor size considered in this study. The contribution of the radiation term increases with increasing temperature but even at a temperature of 1000 degrees Celsius, it is still less than 2%.

Removal of the radiation loss term results in a simpler equation:

$\frac{d^2T}{dx^2}dx = \frac{4h}{kD}(T - T_\infty)dx - \frac{C_g\rho V_0^3 D}{kA_x}dx$ [employing Eq. (3) for Q_f with $a = dx/D$]

$$\Rightarrow \frac{d^2T}{dx^2}dx = \left(0.464\left(\frac{V_o^2 k_f^3 Pr}{\upsilon^2 k_x^3}\right)^{1/3}\times\frac{1}{D^{4/3}}\right)*(T - T_\infty)dx - \left(\frac{C_g\rho V_0^3}{k_x}\right)*\frac{1}{D}dx \tag{13}$$

Let, $A = \left(0.464\left(\frac{V_o^2 k_f^3 Pr}{\upsilon^2 k_x^3}\right)^{1/3}\times\frac{1}{D^{4/3}}\right)\ (1/\mathrm{m}^2)$

and $B = \frac{C_g\rho V_0^3}{k_x} * \frac{1}{D}$ (K/m^2) where C_g = 0.01 for peter correlation [40]

$$\Rightarrow \frac{d^2T}{dx^2} - A*(T - T_\infty) + B = 0$$

Let, $\theta = T - T_\infty$

$$\Rightarrow \frac{d^2\theta}{dx^2} - A\theta + B = 0 \tag{14}$$

This is a non-homogeneous 2nd order ODE yielding the solution

$$\theta = C_1 e^{-mx} + C_2 e^{mx} + \frac{B}{A} \qquad [m = \sqrt{A}] \tag{15}$$

Employing the following boundary conditions

$$at\ \ x = 0,\quad \theta = \theta_H$$

$$at\ \ x = L,\quad \frac{d\theta}{dx} = 0$$

The second boundary condition reflects the fact that the shaft temperature is expected to drop down to the allowable limit at the end of the

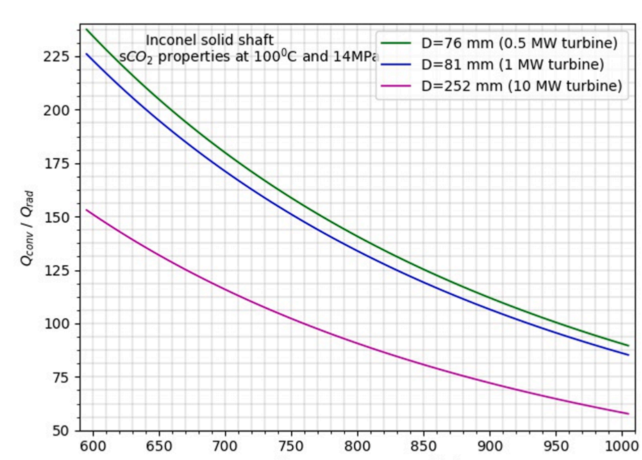

Fig. 5. The ratio of the convective to radiative loss over a unit length of the shaft.

cooling zone and there is no heat transfer into the seal. Applying the boundary conditions, the expression for θ can be obtained as follows:

$$\Rightarrow \frac{\theta - \frac{B}{A}}{\theta_H - \frac{B}{A}} = \frac{cosh\left[\sqrt{A}\,(L-x)\right]}{cosh\left[\sqrt{A}L\right]} \tag{16}$$

where the hyperbolic function is defined as $coshx = \frac{e^x + e^{-x}}{2}$.

Using this equation, Fig. 6 shows the nondimensional temperature distribution as a function of x/D corresponding at three different turbine sizes. The chart has been plotted for Inconel 718 solid shaft and supercritical CO_2 temperatures calculated at the coolant inlet temperature, T_C, as defined in Table 3. The curves for 0.5 MW and 1 MW are almost identical. The 10 MW turbine shows faster cooling characteristics compared with the other two. This may be due to the larger diameter increase in the shaft surface area as well as the cooling area. The shaft surface temperature can be easily evaluated at different T_∞ and T_H temperatures corresponding to different x/D values. For example, for a 0.5 MW turbine size and an axial position of x/D = 0.3, the nondimensional temperature value read from the chart is 0.016. If the rotor backplane temperature is $T_H = 600$ degrees Celsius and for the value of 'A' and 'B' at supercritical CO_2 temperature T_∞=120 degrees Celsius this yields the shaft surface temperature as 217 degrees Celsius.

Until the temperature becomes very high and radiative heat transfer becomes important, the curves plotted in Fig. 6 are independent of the turbine inlet temperature and can be used to analyze cooling zone length requirements at other temperatures. The interesting finding of the above analysis is the fact that the dimensionless temperature is independent of the radial clearance, C. This is because substituting the physical constraints dictated by the equipment limitations listed in Table 3 (maximum allowable dry gas seal temperature, To, and the maximum shaft surface speed, (Vo) allowed us to eliminate the effect of the radial clearance.

This is an interesting finding because the next section explores how the cooling zone can be made to provide additional shaft support against whirling while maintaining an adequate cooling function. Having the radial gap as a degree of freedom in this analysis offers a significant advantage.

4. Mechanical analysis

Mechanical support on the rotating shaft is another important part of the analysis in this study. It will investigate whether it can provide some extra support on the rotating shaft employing annulus cooling length with high-pressure supercritical CO_2 circulating fluid.

The overhung shaft is supported by two bearings on the right (Fig. 2). The high rotational speed and overhung arrangement make an out-of-balance force and lead the rotor shaft to whirl in an elliptical orbit. As the shaft undergoes a whirling motion, the circulating fluid squeezed between the shaft and annulus outer wall produces a reactive force, so-called restoring force, that tries to push the shaft back to its central position. This happens only when the shaft gets closer to the wall. This action is similar to what happens in hydrodynamic bearings. In hydrodynamic bearings, Reynold's theory of hydrodynamic lubrication [44–47] is used to estimate this force. The minimum rotational Reynolds number associated with our application is 4×10^3 falls within the range of Reynolds number typically encountered in hydrodynamic lubrication, which ranges from 2×10^3 to 10^5 [48]. Hence it is expected that Reynolds's theory is useful to provide an approximate answer as explained below. In Reynold's theory, the magnitude of the force is influenced by the annulus gap clearance: the smaller the radial clearance, the higher the magnitude of restoring force. There is a degree of freedom to vary the annulus gap clearance to maximize the support because the thermal design does not place a constraint on gap clearance as per the findings stated in the previous section.

In standard journal bearing theory, restoring force is generated in response to an external static load. In the supercritical CO_2 rotor shaft cooling zone, there is no significant external load being applied on the shaft but the restoring force is generated in response to the whirling displacement of the shaft. When the shaft is not whirling, there is no force. The physical representation of the rotor shaft annulus and the notations are given in Fig. 7.

The shaft displacement and reaction forces are expressed in the fixed (X, Y) coordinate and flexible (r, t) coordinate system. The "X" axis is chosen to align with the load direction (W). The attitude angle ϕ is measured between the load direction and the shaft eccentricity (e). In this instance, there is no external load and the deflection of the shaft is caused by whirling. Therefore, the resultant load direction will be always in the direction of eccentricity. The tangential component of the force will be negligible and therefore the attitude angle will be zero. Fig. 7 was drawn at the instant when the fixed X, Y coordinates coincided with the rotating r, t coordinates.

Different restoring force correlations exist in the literature, including Luis, Kingsbury, and Genta [44,46–47]. They have the common form as given below.

$$W_r = C_d\,\mu V_0 \frac{R^3}{C^2} \times f(\varepsilon) \tag{17}$$

where C_d is a constant.

They are all derived from Reynold's theory of hydrodynamic

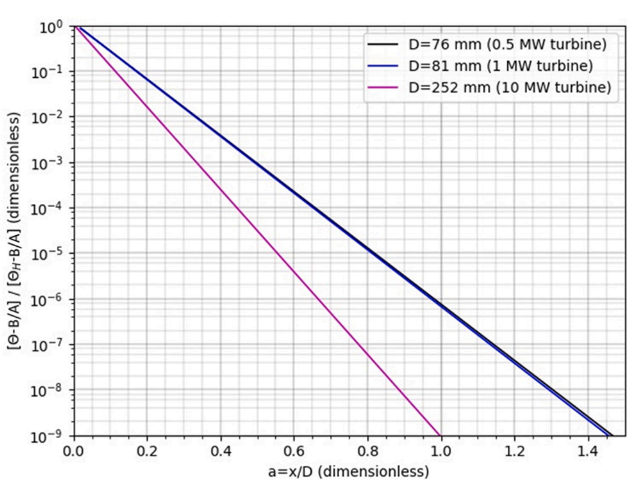

Fig. 6. Temperature distribution over the length of the cooling zone as a function of x/D.

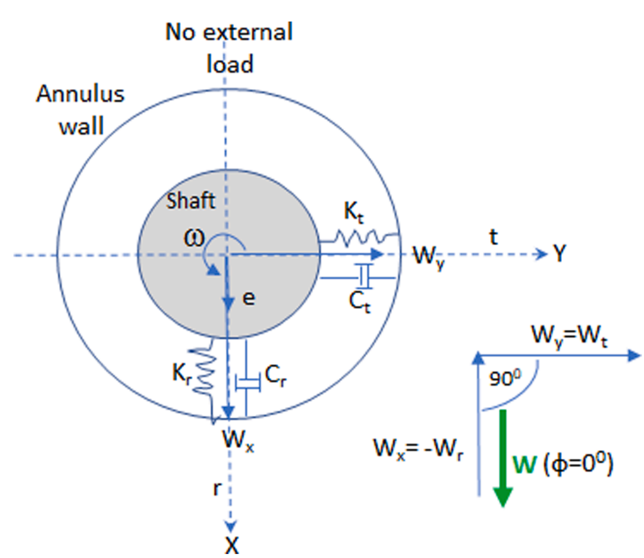

Fig. 7. A physical representation of the rotor shaft annulus and notations.

lubrication assuming laminar flow and neglecting inertial effects. They have been very successful in producing robust and enduring journal-bearing designs used in various applications. A typical journal bearing has a C/R value is 0.001 and maybe rotating at speeds well above 10,000 revolutions per minute and lubricated by the process fluid [46]. The cooling zone proposed in this paper operates at higher speeds but not too far out from the speed range experienced by some of the modern journal bearings. The flow will be turbulent and inertial forces are expected to exceed viscous forces. While the Reynolds theory ignores inertial effects, the influence of inertial effects on hydrodynamic journal bearings has been experimentally investigated and reported that with the rotating fluid particle confined between two surfaces, the centripetal, Coriolis, linear, and angular acceleration components dominate and the inertial effects may be neglected. Therefore, such an annular geometry can carry appreciable loads even with the journal rotating at high speeds [49]. In other applications, the rotational speed of the hydrodynamic journal bearing is limited by the factor of heat generation due to friction [50–53]. This is already accounted for in our analysis in the preceding section.

In the subsequent analysis, the author used the Luis correlation due to the simplicity of the expression, by substituting $L = 2aR$ and $\Omega = V_0/R$, the restoring force corresponding to a radial deflection is estimated as [46].

$$W_r = -\frac{\mu V_0 (aR)^3}{C^2}\left[\frac{8\varepsilon^2}{\left(1-\varepsilon^2\right)^2}\right] \tag{18}$$

The stiffness can be determined by dividing the expression for the force by the displacement. The shaft displacement is known as eccentricity (e).

$$K_c = K_r = \frac{W_r}{e} \tag{19}$$

It would be instructive to express the cooling zone stiffness as a multiple of the stiffness of the rotor shaft as $K_c = \lambda \times K_s$. The magnitude of the coefficient λ then represents a measure of the contribution of the cooling zone stiffness to the overall shaft stiffness. The stiffness of the rotor shaft can be computed by a simple beam analysis. Recall that the rotor shaft is overhung supported by two bearings as shown in Fig. 2. The spring constant for this geometry can be calculated as follows [54]:

$$K_s = \frac{W}{\delta} = \frac{3EI}{\left[D^3\,(1.63+a)^2\,(2.68+a+b)\right]} \tag{20}$$

where ‘E’ is the modulus of elasticity for the shaft material, ‘I’ the area moment of inertia of cross-section of the shaft, *a*, *b*, and *D* represent the geometry as shown in Fig. 2.

Combining Eqs. (19) and (20) and simplifying:

$$\frac{\lambda EIC^3}{a^3R^6V_0\mu L_1^2L_2} = \frac{64}{3}\left(\frac{\varepsilon}{\left(1-\varepsilon^2\right)^2}\right) \tag{21}$$

where $L_1 = (1.63 + a)$and $L_2 = (2.68 + a + b)$.

The term on the left-hand side is a dimensionless term that is a function of the geometry and material properties and can be used as a measure of cooling zone stiffness. Fig. 8 shows how this dimensionless number varies with eccentricity ratio ($\varepsilon = e/C$). At zero whirl, the eccentricity is zero and so is the stiffness. Stiffness increases with increasing eccentricity ratio, which is a manifestation of rotor whirl. As the whirling rotating shaft approaches the annulus wall, there is a rapid increase in stiffness.

Fig. 8 can be used by the radial turbine designer to evaluate the lambda value as a function of the eccentricity ratio (i.e. the whirl amplitude) at different geometrical and operating parameters. As an example, assume a 0.5 MW rotor size, a cooling flow inlet temperature of 180 degrees Celsius, and a radial clearance of $C = 0.001R$. The non-dimensional value $\varepsilon = 0.95$ can be read from the chart as 1853. If the width of the cooling zone is $a = 0.5D$ and the bearing spacing is $b = 1D$ and using Inconel ($E = 1.66 \times 10^{11}\,\mathrm{N/m^2}$), this gives a value of λ is 1.0. This means that the cooling zone for the stated configuration doubles the stiffness of the rotor shaft and can make a significant contribution to rotor dynamic analysis.

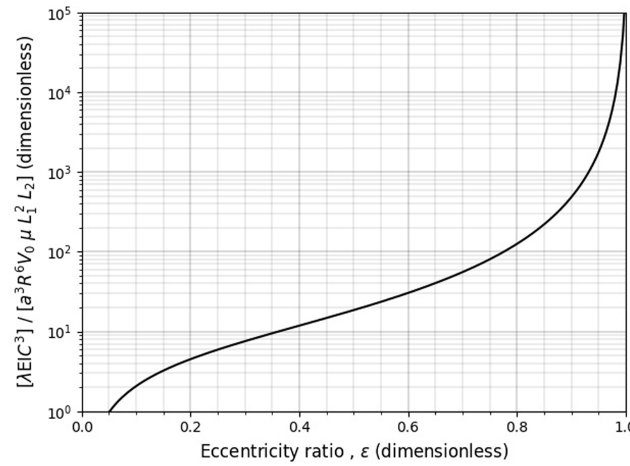

Fig. 8. Dimensionless lambda value as a function of eccentricity ratio.

5. Rotor dynamic analysis

The analysis of vibration frequencies and critical speeds are the essential design acceptance criteria of the high-speed turbine rotor system. The vibration mode consists of two components as forwarding mode and backward mode. The intersection between the excitation frequency line and the vibration/natural frequency line is used to determine the critical speed of the system. Supercritical CO_2 turbine rotor shafts have very high rotational speeds and the natural frequencies need to avoid the blade excitation frequencies that correspond to the rotational speed and its subharmonics. The Campbell diagram is one of the important tools to understand and analyze such rotor dynamic behavior. COMSOL rotor-bearing system simulator has been used to generate the Campbell diagram in this study. The parametric study has been conducted for the geometry of the rotor support essential element shown in Fig. 2.

5.1. Simulation details

The rotor-bearing system simulator consists of bearings and disks attached to the rotating shaft. The Campbell plot, whirl mode plot, and the critical speeds are the results of the COMSOL analysis. The geometry has been modified by the parameters and assumptions given in Table 5 related to the rotor, disk, bearings, and configuration. The rotor is modified by the geometric dimensions and material properties. The circular disk with center hole diameter is equal to the outer diameter of the shaft is modified by the inertial properties. The inertial properties are computed by the following expressions [55].

$$m_d = \rho\pi\left(\frac{d_d^2 - D_o^2}{4}\right)h_d \tag{22}$$

$$I_p = m_d\left(\frac{d_d^2 + D_o^2}{8}\right) \tag{23}$$

$$I_d = m_d\left(\frac{d_d^2 + D_o^2}{16} + \frac{h_d^2}{12}\right) \tag{24}$$

where m_d the mass of the disk, I_p the polar moment of inertia, I_d the diametral moment of inertia, D_o the outer diameter of the shaft, h_d the thickness of the disk, d_d the outer diameter of the disk. The values of the

Table 5
Study configurations and rotor parameters.

Config.	Cooling length factor, a	Bearing spacing factor, b	0.5 MW turbine		10 MW turbine		Bearings and rotor disc
			Radial clearance, C (mm)	Cooling length spring constant, λ	Radial clearance, C (mm)	Cooling length spring constant, λ	
1a	1.0	1.58	0.04	15.0	0.12	4.5	– Tilted pad bearing stiffness 5.3×10^8N/m [56]
1b			0.06	4.0	0.16	2.0	
1c			0.08	1.5	0.25	0.5	– Inconel shaft diameter 76 mm and 152 mm for the 0.5 MW and 10 MW turbine respectively
2a	2.0	2.58	0.04	321	0.12	92	
2b			0.06	79	0.16	40	– Rotor disc mass 10 kg and 382 kg for the 0.5 MW and 10 MW respectively [30]
2c			0.08	33	0.25	10	– perating speed 3141 and 900 rad/s for 0.5 MW and 10 MW respectively

disk geometry have been adopted from Ref. [30].

The effects of using different cooling zone lengths and bearing spacings are examined. These different geometry configurations are considered with three radial clearance values chosen from the range of clearance ratios typically encountered in journal bearings. The corresponding λ values were computed to investigate the contribution of cooling length to rotor dynamics. A one-fold decrease in the radial clearance impact is a two-fold increase in the lambda value (Table 5).

5.2. Simulation outcome

Campbell charts are the tools traditionally used to avoid possible turbomachinery vibration problems. The Campbell charts have been constructed for the configurations listed in Table 5. Fig. 9 shows an example. The x-axis represents the shaft speed, Ω, and the y-axis the natural frequency. Two first-order solutions to the shaft vibration equation correspond to forward synchronous whirl and backward synchronous whirl. Forward synchronous whirl is the most common in practice but under certain anisotropy conditions such as oil film bearings and anisotropic rotors, it is possible to get backward whirl motion. Both whirl frequencies are shown in the Campbell chart. They do not change much with the rotational speed. Only the forward whirl will be considered in the analysis below. The sloping lines in Fig. 9 are examples of excitation frequencies and are referred to as excitation frequency lines. The main excitation is the rotational speed, i.e. the line at $\omega = \Omega$. The others for $\omega = 2\ \Omega$ and $\omega = 0.5\ \Omega$ result from the fluid-rotor interactions, for example, the blade passes. There are usually many of the latter that needs to be considered but only two are shown in Fig. 9 to avoid clutter. An intersection of a whirl frequency line with an excitation frequency line is to be avoided because it corresponds to a resonant condition.

The purpose of the present analysis is to show how one can ascertain the effect of the cooling zone design on the rotor shaft vibrations. Therefore, it is sufficient to focus only on the main excitation frequency line ($\omega = \Omega$). The intersections of the main excitation frequency line with the forward whirl frequencies have been computed for all configurations listed in Table 5 and the results are shown in Table 6.

As expected, the addition of the cooling length stiffness to a 0.5-MW rotor design results in a stiffer shaft by about 13–42% for a dimensionless cooling length of $a = 1.0$ and 47–55% for $a = 2.0$, where a is the dimensionless cooling zone length. The numbers are similar for a 10-MW turbine size. A stiffer rotor shaft makes it easier to tailor the overall rotating assembly stiffness by, if necessary, manipulating the support stiffnesses. Therefore, a stiff shaft is preferable to a floppy shaft. In other words, the design of a cooling zone with intrinsic stiffness results in a significantly better outcome.

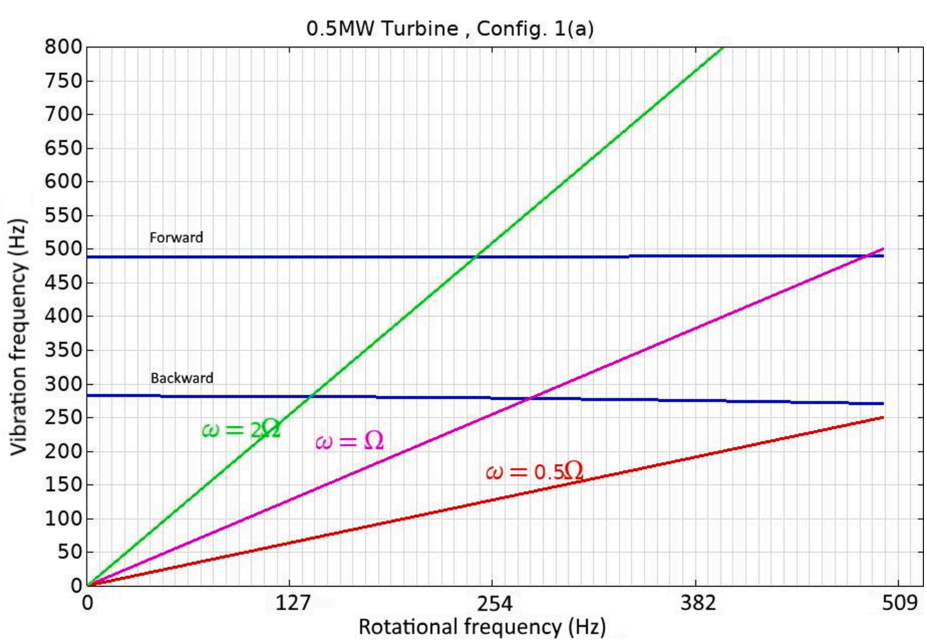

Fig. 9. Campbell diagram for a 0.5 MW-turbine size and configuration 1a (as in Table 5).

Table 6
Quantitative results of dynamic performance.

Turbine size	Configurations	The critical shaft speed with cooling length stiffness (Hz)	The critical shaft speed without cooling length stiffness (Hz)	Dynamic performance improved
0.5 MW	1a	489	283	13–42%
	1b	385		
	1c	325		
	2a	427	190	47–55%
	2b	399		
	2c	359		
10 MW	1a	114	63	12–45%
	1b	93		
	1c	72		
	2a	119	49	45–60%
	2b	112		
	2c	90		

6. Trade-offs in designing the cooling zone

Trade-off analysis is essential in this study for prioritizing among the dual requirements such as shaft cooling and dynamic support. It is required to cool the rotor shaft and at the same time provide adequate dynamic support against the vibration under certain conditions.

To cool the rotor shaft up to the desired temperature mentioned in the earlier sections, the total amount of heat required to remove can be computed by the following expression.

$$Q_T = Q_c + Q_f = k\frac{\pi D}{4a}(T_H - T_0) + C_g \rho V_0^3 D^2 a \tag{25}$$

The cooling capacity through circulating the supercritical CO_2 coolant can be computed by the following expression.

$$q_c = \dot{m} C_p \Delta T \tag{26}$$

By introducing the definition of the axial Reynolds number, Re_a:

$$q_c = 0.5\pi\mu C_p.\ Re_a\,(2R + C).\ (T_H - 353) \tag{27}$$

Combining Eqs. (24)–(27), the trade-off relationships between different parameters as shown in Fig. 10 for two rotor sizes, 0.5 MW, and 10 MW. Inconel shaft materials and the coolant properties at 80 degrees Celsius and a pressure of 14 MPa are assumed. The Taylor number in this study Ta $> 10^6$ followed the axial Reynolds number is 2.5×10^4 recommended [43] and the eccentricity ratio is 0.9 for maximum dynamic support has been used.

The total heat supposed to remove from the cooling zone includes conduction heat and frictional heat does not depend on the radial

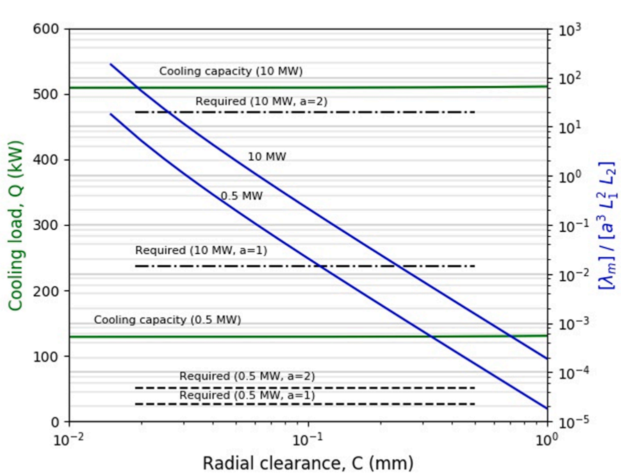

Fig. 10. Trade-offs in designing the cooling length.

clearance and are marked by the dotted line at different cooling length factor for 0.5 MW and 10 MW turbine size. The cooling capacity depends on the radial clearance and is plotted in the green line for 0.5 MW and 10 MW turbine size. It is seen that the cooling capacity curve is almost flat due to the insignificant effect of change of clearance on the cooling capacity. The figure shows that the cooling capacity is always higher than the cooling required. However, the cooling capacity is greatly influenced by the axial Reynolds number. The figure implies that the designer has a degree of freedom to vary the radial clearance to maximize the maximum dynamic support. The higher the radial clearance lower the dynamic support plotted by the blue line for 0.5 MW and 10 MW turbine size. The chart can be used for optimizing the dynamic support for a given rotor design. For example, the maximum lambda (λ_m) value read from the chart is 8.1127 $\times$ 10^{-3}. If the cooling length factor a = 1.5 for b = 2.08 leads the λ_m value is unity at C = 0.13 mm and C = 0.30 mm for 0.5 MW and 10 MW turbine size respectively. The axial coolant velocity at Reynolds number 2.5×10^4 and coolant properties at 80 degrees Celsius, 14 MPa computed are 7.43 and 3.22 m/s for the 0.13 and 0.30 mm clearances respectively.

7. Conclusion

This article follows the recent developments of supercritical CO_2 energy generation radial turbine technology. The bearing and seal design were found as critical challenges due to the high temperature, high pressure, and high rotational speed of the supercritical CO_2 turbine. A newly designed turbine configuration was adopted in this study to defend against such challenges. This configuration allows the use of proven dry gas seal and journal bearing technology with supercritical CO_2 turbines. To isolate the seals and bearings from high temperatures, a rotor shaft cooling zone is proposed, which cools the rotor shaft while introducing additional unsupported length. The purpose of this study is to offer a parametric model to radial supercritical CO_2 turbine designers in designing this cooling zone with a dual purpose: cool the rotor shaft and provide dynamic support to the against vibrations. The following conclusions are summarized from this study.

(1) While radiation heat transfer can be ignored, the contribution of frictional heat generation to the cooling load is significant.
(2) The relatively high value of the convection heat transfer coefficient makes it possible to achieve the required cooling in a shaft length of one to two diameters. The convection heat transfer coefficient and the dimensionless temperature distribution are independent of radial clearance.
(3) Hydrodynamic lubrication theory and simplified correlations have been employed to investigate the magnitude of dynamic support in terms of shaft stiffness. It is found that the behavior of the dimensionless stiffness contribution is a non-linear function of the shaft eccentricity ratio.
(4) The generalized design chart has been constructed in terms of the dimensionless number to facilitate a wide variety of turbine size applications and support optimization.
(5) The rotor dynamic vibration frequencies are analyzed using Comsol software. Campbell diagrams were plotted for a range of cooling zone configurations and support lengths. The cooling zone is found to contribute to the shaft stiffness by 55% to 60% for 0.5 MW and 10 MW rotors, respectively.
(6) For the values considered, the annular clearance does not affect the cooling capacity but has a large influence on the stiffness. This provides the designer with considerable freedom in designing the rotor assembly in a way to avoids resonance conditions.

The generalized charts and the equations presented in this paper can be used by the turbine designer to find the optimum trade-off between the rotor shaft stiffness and the temperature limitations while designing a supercritical CO_2 radial in-flow turbine. Further investigation will be done using computational fluid dynamics to validate the assumptions behind the above conclusions.

Declaration of Competing Interest

The authors declare that they have no known competing financial interests or personal relationships that could have appeared to influence the work reported in this paper.

Acknowledgement

Uddin would like to thanks the University of Queensland and the Australian Solar Thermal Research Institute (ASTRI) for providing the appropriate platform and funding for this study.

References

[1] International Energy Agency. Electricity statistics: Detailed, comprehensive annual data on electricity and heat. Available online: https://www.iea.org/statistics/electricity/ (Retrieved 27 September 2018).
[2] V. Dostal, M.J. Driscoll, P. Hejzlar, A supercritical carbon dioxide cycle for next generation nuclear reactors, The MIT Center for Advanced Nuclear Energy Systems, USA, 2004, pp. 1–300.
[3] M.C. Thomas, A.W. Steven, E.A. Davit, G.L. Tom, CO2-Based Mixtures as Working Fluids for Geothermal Turbines, Sandia National Laboratories, USA, 2012, p. 40.
[4] T.M. Conboy, M.D. Carlson, G.E. Rochau, Dry-cooled supercritical CO_2 power for advanced nuclear reactors, J. Eng. Gas Turbines Power 137 (1) (2015), 012901-1-10.
[5] H. Gurgenci, Supercritical CO2 cycles offer experience curve opportunity to CST in remote area markets, in: International Conference on Solar Power and Chemical Energy Systems (SolarPACES 2013), Las Vegas, United States.
[6] US Department of Energy Supercritical CO2 Team, Available online: https://www.energy.gov/supercritical-co2-tech-team (Retrieved 19 December 2020).
[7] Evan P. Reznicek, Design and simulation of supercritical CO2 recompression Brayton cycles with regenerators for recuperation. Ph.D. thesis. Department of Mechanical Engineering, Colorado school of mine university, USA, 2019.
[8] Sunshot Vision Study 2012- US Department of Energy. Available online: https://www.energy.gov/eere/solar/sunshot-vision-study.
[9] C.S. Turchi, Supercritical CO2 for application in concentrating solar power systems, in: Supercritical CO2 Power Cycle Symposium. Troy, NY, 2009.
[10] A. Fahad, A. Sulaiman, A. Maimoon, Performance comparison of different supercritical carbon dioxide Brayton cycles integrated with a solar power tower, Energy 82 (2015) 61–71.
[11] R. Chacartegui, J.M. Muñoz de Escalona, D. Sánchez, B. Monje, T. Sánchez, Alternative cycles based on carbon dioxide for central receiver solar power plants, Appl. Therm. Eng. 31 (5) (2011) 872–879.
[12] T. Neises, C. Turchi, A comparison of supercritical carbon dioxide power cycle configurations with an emphasis on CSP applications, Energy Procedia 49 (2014) 1187–1196.
[13] W. Kun, L.H. Ya, H.Z. Han, Integration between supercritical CO_2 Brayton cycles and molten salt solar power towers: A review and a comprehensive comparison of different cycle layouts, Appl. Energy 195 (2017) 819–836.
[14] S.K. Min, A. Yoonhan, K. Beomjoo, I.L. Jeong, Study on the supercritical CO_2 power cycles for landfill gas firing gas turbine bottoming cycle, Energy 111 (2016) 893–909.
[15] L. Dan, L. Yu, S. Xiaojing, H. Diangui, The design and analysis of supercritical carbon dioxide centrifugal turbine, Appl. Therm. Eng. 127 (2017) 527–535.
[16] H. Norman, B. Giuseppe, D.M. Maxence, S.S. Samira, A.T. Savvas, L. Arthur, J. Hussam, Design of radial turbomachinery for supercritical CO_2 systems using theoretical and numerical CFD methodologies, Energy Procedia 123 (2017) 313–320.
[17] Q. Jianhui, R. Thomas, Q. Kan, H. Kamel, H.J.J. Ingo, Supercritical CO_2 Radial Turbine Design Performance as a Function of Turbine Size Parameters, J. Turbomachinery 139 (8) (2017) 1–11.
[18] H. Alexander, S. Sebastian, J.D. Hans, K.B. Friedrich, B. Dieter, Turbomachine Design for Supercritical Carbon Dioxide Within the sCO2-HeRo Project, J. Eng. Gas Turbines Power 140 (12) (2018) 1–8.
[19] Apostolos A. Gkountas, Anastassios M. Stamatelos, Anestis I. Kalfas, Recuperators investigation for high-temperature supercritical carbon dioxide power generation cycles, Appl. Therm. Eng. 125 (2017) 1094–1102.
[20] Alan Wright Steven, F. Radel Ross, E. Vernon Milton, S. Pickard Paul, Eugene Rochau Gary, Operation and analysis of a supercritical CO2 Brayton Cycle, Sandia National Laboratories, 2010. p. 101.
[21] K.J. Kimball, E.M. Clementoni, Supercritical carbon dioxide brayton power cycle development overview, ASME Turbo Expo 2012, Copenhagen, Denmark.
[22] Motoaki Utamura, Hiroshi Hasuike, Kiichiro Ogawa, Takashi Yamamoto, Toshihiko Fukushima, Demonstration of supercritical CO2 closed regenerative Brayton cycle in a bench-scale experiment, ASME Turbo Expo, 2012, Copenhagen, Denmark.
[23] Jishun Li, Hal Gurgenci, Zhiqiang Guan, Jun Li, Md. Shazib Uddin, Lun Li, Bearing and seal selection for a high-temperature supercritical CO2 turbine, Proc. Global Power Propulsion Soc. (Beijing Conference), 2019.
[24] A.W. James, S. Rajagopalan, Gas turbines: operating conditions, components, and material requirements, Struct. Alloys Power Plants (2014) 3–21.
[25] Yoonhan Ahn, Seong Jun Bae, Minseok Kim, Seong Kuk Cho, Seungjoon Baik, Jeong Ik Lee, Jae Eun Cha, Review of Supercritical CO2 Power Cycle Technology and Current Status of Research and Development, Nucl. Eng. Technol. 47 (2015) 647–661.
[26] Shinko Industries limited. Steam turbines for Industries, 2017, Japan.
[27] T.C. Allison, J. Moore, R. Pelton, J. Wilkes, B. Ertas, Fundamentals, and applications of supercritical carbon dioxide (sCO2) based power cycles, Turbomachinery (2017) 147–215.
[28] R. Aaron, S. Natalie, W. Jason, D. Hector, A. Timothy, A.B. Rahul, K. Uttara, T. Deepak, Test rig design for large supercritical CO2 turbine seals, in: The 6th International Supercritical CO2 Power Cycles Symposium, Pittsburgh, Pennsylvania, March 27-29, 2018.
[29] P.B. Swann, H. Russell, Rotating Shaft Thermal Analysis for Supercritical Carbon Dioxide Radial Inflow Turbines, in: 15th International Energy Conversion Engineering Conference, 2017, Atlanta, Georgia.
[30] Sangkyoung Lee, Hal Gurgenci, A Comparison of Three Methodological Approaches for Meanline Design of Supercritical CO2 Radial Inflow Turbines, Energy Conv. and Manag. 206 (2020) 112500, https://doi.org/10.1016/j.enconman.2020.112500.
[31] C. Filippo, C. Steven, P. Paolo, N. Leonardo, C. Lorenzo, Thermo-elasto bulk-flow model for labyrinth seals in steam turbines, Tribol. Int. 119 (2018) 359–371.
[32] J.L. Jeong, Y.K. Soo, S.K. Tong, S.B. Sam, Thermo-economic analysis on the impact of improving inter-stage packing seals in a 500 MW class supercritical steam turbine power plant.*Applied*, Therm. Eng. 121 (2017) 974–983.
[33] A.Z.M. Fairuz, J. Ingo, A.R. Razi, The effect of convection area on the deformation of dry gas seal operating with supercritical CO2, Tribology Int. 137 (2019) 349–365.
[34] Xuexing Ding, Junjie Lu, Theoretical analysis, and experiment on gas film temperature in a spiral groove dry gas seal under high speed and pressure, Int. J. of Heat and Mass Transfer 96 (2016) 438–450.
[35] H. Thomas, P. Peter, S. Hubert, Measured and Predicted Operating Characteristics of a Tilting-Pad Journal Bearing with Jacking-Oil Deviceat Hydrostatic, Hybrid, and Hydrodynamic Operation, Lubricants 6 (81) (2018) 1–15.
[36] D. Karl, R. Wygant, D. Flack, E.B. Lloyd, Measured Performance of Tilting-Pad Journal Bearings over a Range of Preloads—Part I: Static Operating Conditions, Tribol. Trans. 47 (4) (2004) 576–584.
[37] F. Michel, B. Jean, F. Jean, Experimental study of tilting pad journal bearing-comparison with theoretical thermoelastic-hydrodynamic results, J. Tribol. 114 (1992) 579–587.
[38] K.D. Maglic, N.L. Perovic, A.M. Stanimirovic, Calorimetric and transport properties of zircalloy 2, Zircalloy 4, and Inconel 625, Int. J. Thermophys. 15(4) (1994) 741–755.
[39] J.N. Sweet, E.P. Roth, M. Moss, Thermal conductivity of Inconel 718 and 304 stainless steel, Int. J. Thermophsics 8(5) (1987) 593–606.
[40] R.N. Peter, Rotating flow: Chapter 6-Rotating cylinders, annuli, and spheres. Rotating flow, Elsevier, 177–247.
[41] Ralph A. Burton, in: Heat, Bearings, and Lubrication, Springer New York, New York, NY, 2000, pp. 60–67, https://doi.org/10.1007/978-1-4612-1248-5_8.
[42] E.V. James, Prediction of windage power loss in Alternators, Lewis Research Center Cleveland Ohio: the USA, 1968, 1–18.
[43] M. Fenot, Y. Bertin, E. Dorignac, G. Lilezel, A review of heat transfer between concentric rotating cylinders with or without axial flow, Int. J. Therm. Sci. 50 (2011) 1138–1155.
[44] Kingsbury, Optimum conditions in Journal Bearings, Transac. Am. Soc. Mech. Eng. 54 (1932) 123–148.
[45] K. Evgueni, M.M. Alison, Bearing out of balance stability-A comparison of restoring force models, ISCORMA-3, Cleveland, Ohio, 2005, 1–18.
[46] S.A. Luis, Hydrodynamic fluid film bearing and their effect on the stability of rotating machinery. Educational Notes RTO-EN-AVT-143; Neuilly-sur-Seine: France, 2006, Paper 10, 1-35.
[47] G. Giancarlo, Rotor bearings interaction, in: Dynamics of rotating systems, Springer, USA, 2005, 281–317.
[48] F. Jean, A. Mihai, C. Virgil, Combined thin-film and Navier-Stokes analysis in high Reynolds number lubrication, Tribology Int. 39 (2006) 734–747.
[49] C.S. Milton, D.S. Chalres, Role of inertia in hydrodynamic lubrication, J. Nat. 158 (1946) 452.
[50] S.A. McKee, Journal-bearing design as related to maximum loads, speeds, and operating temperatures, J. Res. Natl. Bureau Standards 19 (4) (1937) 457, https://doi.org/10.6028/jres.019.027.
[51] Hydrodynamic Lubrication, Industrial Lubrication, and Tribology. MCB UP Ltd: UK, 1957, Vol. 9 Issue: 12,75-101. https://doi.org/10.1108/eb052495.
[52] American Roller Bearing Company. Speed limits of bearing. Available online: https://www.amroll.com/speed-limits.html (Retrieved 24 April 2019).
[53] H. Xiao, W. Li, Z. Zhou, X. Huang, Y. Ren, Performance analysis of aerostatic journal micro-bearing and its application to high-speed precision micro-spindles, Tribol. Int. 120 (2018) 476–490.
[54] L.M. Robert, M.V. Edward, J. Wang, Machine Elements in Mechanical Design, 6th ed., Pearson, New York, 2018.
[55] COMSOL rotodynamic application 5.5. Rotor bearing system simulator, pp1-4.
[56] B.P. Heinz, Improving machinery reliability Volume 1 (1998) 90.